# Simulation of vortex pair instabilities behind a split wing

Pierre Saulgeot, Vincent Brion, Navrose Navrose, Nicolas Bonne, Laurent Jacquin, Emmanuel Dormy

# Simulation of vortex pair instabilities behind a split wing

Pierre Saulgeot* and Vincent Brion†
*ONERA, Université Paris-Saclay, 8 rue des Vertugadins, F-92190 Meudon, France*

Navrose‡
*Indian Institute of Technology, Kanpur, Kanpur 208 016, UP, India*

Nicolas Bonne§ and Laurent Jacquin¶
*ONERA, Université Paris-Saclay, 8 chemin de la Hunière, FR-91123 Palaiseau, France*

Emmanuel Dormy‖
*École Normale Supérieure, CNRS, PSL University, F-75005 Paris, FRANCE*

**The dynamics of a pair of counter-rotating wingtip vortices formed in the wake of a slotted wing are investigated numerically at Reynolds numbers 3000 to 10 000, considering a NACA12 airfoil with various angles of attack ranging from 5 to 10 degrees. Two parts of the wake are investigated. Firstly, we focus on the von Kármán wake of the wing and explore its properties in reference to inifinite wing results. The finiteness of the wing introduces notable differences. Secondly, we examine the dynamics of the wingtip vortices and the instabilities that are obtained. The influence of the von Kármán wake on this vortex is emphasized. Two behaviors are identified, depending on the angle of attack and Reynolds number. An orthogonal proper orthogonal decomposition (POD) is applied to identify the coherent structures that superimpose upon the mean flow. A Fourier analysis of the vortex centerline is conducted to highlight the dominant wavelengths.**

## I. Nomenclature

| | | |
|---|---|---|
| $x$ | = | Longitudinal (streamwise) coordinates |
| $y$ | = | Transversal (spanwise) coordinates |
| $z$ | = | Vertical coordinate |
| $b$ | = | Vortex spacing (time dependant) |
| $b_0$ | = | Wing spacing |
| $2s$ | = | Wing span |
| $c$ | = | Wing chord |
| $AR = 2s/c$ | = | Wing aspect ratio |
| $\Gamma$ | = | Vortex circulation (time dependant) |
| $a$ | = | Vortex core radius |
| $\boldsymbol{u}$ | = | Fluid velocity |
| $U_\infty$ | = | Mean flow velocity |
| $\boldsymbol{\omega}$ | = | Fluid vorticity |
| $p$ | = | Pressure |
| $\mathrm{Re}_c$ | = | Chord-based Reynolds number |
| $\mathrm{Re}_\Gamma$ | = | Circulation-based Reynolds number |
| $\alpha$ | = | Angle of attack |

*PhD Student, Aerodynamics Aeroelasticity Acoustics Departement, pierre.saulgeot@onera.fr
†Research Engineer, Aerodynamics Aeroelasticity Acoustics Departement, vincent.brion@onera.fr
‡Assistant Professor, Department of Aerospace Engineering, navrose@iitk.ac.in
§Research Engineer, Multi-Physics Department for Energy, nicolas.bonne@onera.fr
¶Professor, Scientific Director of the fluid mechanics and energetics domain, laurent.jacquin@onera.fr
‖Research Director, Département de Mathématiques et Applications, UMR-8553, emmanuel.dormy@ens.fr

## II. Introduction

The dynamics of vortex pairs is a topic of major importance in the aeronautical community. For instance, aircraft wake vortices are a threat to following aircraft in areas of dense traffic, typically in the take-off and landing lanes of busy airports. The long life span of these vortices imposes to keep large distances between aircraft. This affects the efficiency of air traffic control in the densier airports. Reducing the lifespan of trailing vortices is an effective way to meet the ever-increasing demand for air transport. The lifetime of wake vortices is also a matter of importance for the climate impact of aviation as it affects the altitude and density of contrails [1, 2] when they form under certain types of atmospheric conditions.

Wake vortices typically roll up within 10 wingspans behind an aircraft, forming a quasi-axisymmetric vortex dipole characterized by the circulation $\Gamma$ of the vortices and their separation $b$. In an environment where turbulence and atmospheric stratification are low, the dipole retains its shape as it descends through the atmosphere by self-induction. A few hundred wingspans behind the aircraft, instabilities appear, most often the Crow instability [3] and the elliptical instability [4].

The Crow instability, which can be observed in the sky on a clear day when contrails are captured in the wake vortices [5, 6], is a symmetrical sinusoidal instability. It has a long wavelength (typically 8 times the average distance between the vortices) and develops in a plane rotated by an angle between 40° and 50° with respect to the plane initially containing the two vortices. It is amplified by mutual induction in an exponential way and the nonlinear dynamics can make rings appear when the level of turbulence is low enough. This instability has been reproduced experimentally behind a wing [7–9]. Following Crow and Bate's example [10], various numerical studies have tried to amplify it, by optimal perturbation [11] or by interacting a system of four vortex filaments [12–16].

The elliptical instability is a shortwave instability that occurs when a longitudinal vortex is subjected to a shear velocity field in the plane orthogonal to the axis of the vortex. It occurs in particular in vortex rings [17] where the shearing occurs on the ring due to its own velocity field, and for pairs of longitudinal vortices [4, 18] where the shearing on each of the vortices is produced by the velocity field of the other. It consists of the resonance of Kelvin modes of the same axial wavenumber $k$ and azimuthal wavenumbers $m$ and $m+2$. The $m=-1$ and $m=1$ modes are dominant in the absence of axial flow or if it is weak [18], but they can disappear in favor of the $m=-2$ and $m=0$ modes, or even $m=-3$ and $m=-1$ if the axial flow becomes too significant [19]. The elliptic instability is encountered in pairs of vortices in symmetric and antisymmetric form, with the latter being dominant for the first mode $ka \simeq 2.3$ [20], where $a$ is the vortex dispersion radius. The following modes are found at around $ka \simeq 4$, 5.6 and 7.3.

In this study, we use a classical configuration [21, 22] consisting in placing two wings of the same shape and aligned along the span wise direction close to each other, tip to tip. This setup allows to decorrelate the amplitude of the vortices and the distance between them, and thus to increase the importance of their interaction by bringing them closer together than if they were emitted on either side of the same wing. The instabilities therefore grow faster in physical space, and this makes it possible to reduce the development length required downstream of the wing, making the spatial development accessible to numerical and experimental wind tunnel simulations. These principles are directly dran from the growth rate of these instabilities, which is governed by their growth is governed by the characteristic time [23]

$$\tau = \varepsilon^{-1} = \frac{2\pi b^2}{\Gamma} \tag{1}$$

where $\varepsilon$ is the strain rate.

We fix a Reynolds number between 3000 and 10 000 which allows us to disregard turbulence modeling. Although the Reynolds number is approximately 20 to 100 times greater in a real flow, the very low dissipation of the vortices allows the replication of these instabilities for these lower values. Moreover, there is a recently renewed interest in the wake of lifting wings at low Reynolds numbers for biological (insect flight) and industrial (small flying objects) motivations, as highlighted by [24]. For this range of Reynolds numbers, a Von-Kármán vortex street is formed in the wake and can take various shapes [24–27].

The outline of the paper is the following: section III describes the model of the flow and the numerical setup, section IV analyses the Bénard–von Kármán wake observed just behind the wing and compares our results with the litterature for mesh validation purposes, section V describes the formation of the tip vortex and the mean flow properties, and section VI describes the various observed convective instabilities of the tip vortex.

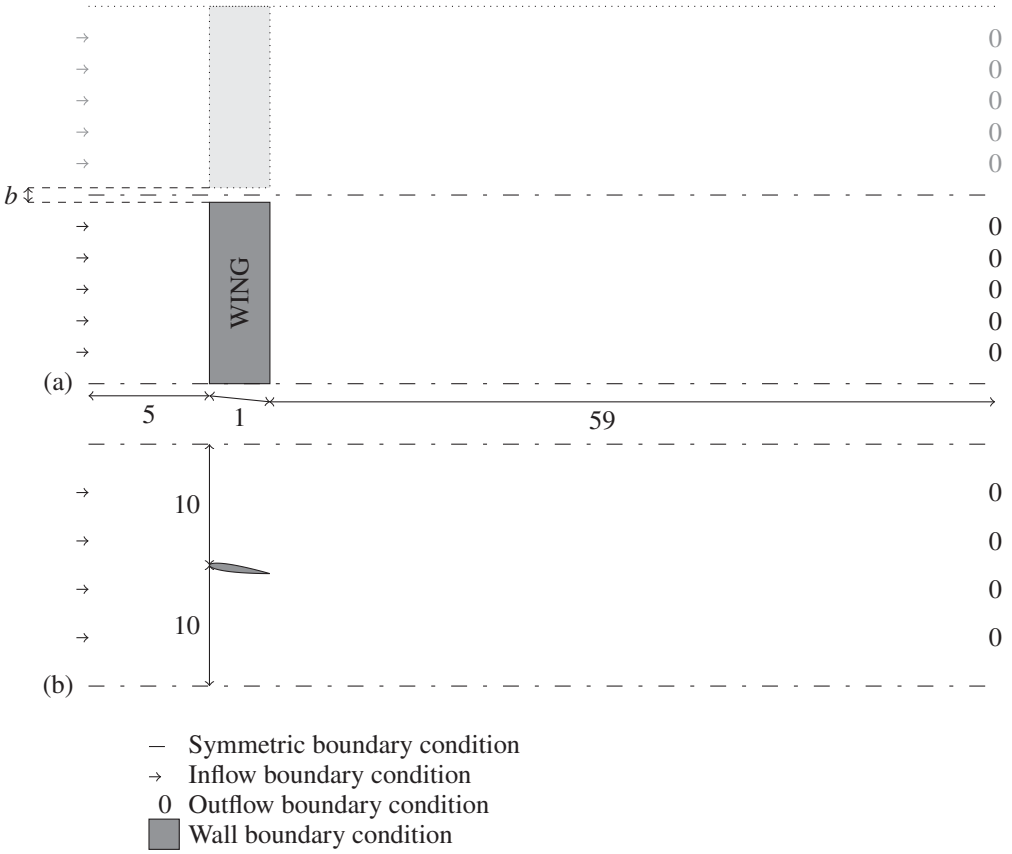


**Fig. 1 (a) Horizontal and (b) vertical slice of the flow domain in the flat plate case. The figure is not to scale. The wing depicted as a light gray shade and the dotted lines represent the configuration as seen by the flow due to the symmetry condition.**

## III. Model

The numerical setup is shown in fig. 1. A NACA0012 airfoil of nonzero angle of attack $\alpha$ with a chord length of $c$ and an aspect ratio of $AR = 6$ is placed in the flow. In the direction of the flow, the domain extends from 5 chords upstream of the wing to 59 chords downstream. The boundary conditions are an incoming flow at a given velocity upstream and an outgoing flow downstream. In the transverse horizontal direction, the domain boundaries are perpendicular to the wing. One lateral boundary lies at the wing root. The other lies at half the wing separation distance from the wing tip. The fluid satisfies symmetry conditions at each of these boundaries. The one slightly offset from the wing tip is denoted as the symmetry plane. Thus, the two-wing configuration is reproduced by symmetry. The top and bottom walls are located far away from the wing, with a distance of 10 times the wing chord. The wake of the NACA0012 airfoil is investigated at an angle of attack of 5, 8 and 10 degrees. The spacing between the wing and the symmetry plane is fixed at 0.12 chord lengths.

Two definition of the Reynolds number are relevant for this problem: the first one based on the chord length $c$ and the incoming free-stream velocity $U_\infty$, and the second one based on the circulation $\Gamma$ of the vortices and their spacing $b$. The first one, expressed as $\mathrm{Re}_c = \frac{U_\infty c}{\nu}$, with $\nu$ the kinematic viscosity, is used to parameterize and initialize the numerical calculation. However, it does not take into account the shape of the wing or the angle of attack. We vary it between 3000 and 10 000. The latter factors have an influence on the wing lift, and hence the strength of the vortices, the separation of the flow over the upper surface, and the appearance of turbulence, as well as the effective surface area of the obstacle as seen by the flow, which may result in a Von Kármán wake. The circulation-based Reynolds number, expressed as $\mathrm{Re}_\Gamma = \frac{\Gamma}{2\pi\nu}$ takes into account the lift and spacing between the vortices (which, as a reminder, is independent of the wing span in our configuration), and is therefore the number that best characterizes the physics of the interaction between the two vortices. An approximation of this Reynolds number can be calculated *a priori*, but it can only be determined once the simulation is performed, as it depends on the distance behind the wing at which the vortex is evaluated. The relationship between the two Reynolds numbers is given by the following equation

$$\frac{\mathrm{Re}_\Gamma}{\mathrm{Re}_c} = \frac{\Gamma}{2\pi c U_\infty}, \tag{2}$$

where $\Gamma$ is the only variables that need to be measured. A preliminary estimate for $b$ once the vortex sheet is rolled up (in the framework of lifting-line theory, see [23]), can be given by $b = b_0 + \left(1 - \frac{\pi}{4}\right) s$. In the case where $b_0 = 0.24$ and $s = 3$, this yields $b = 0.88$

The governing equations are the incompressible Navier-Stokes equations, given here in dimensionless form:

$$\boldsymbol{\nabla} \cdot \boldsymbol{u} = 0, \tag{3a}$$

$$\frac{\mathrm{d}\boldsymbol{u}}{\mathrm{d}t} = -\boldsymbol{\nabla} p + \frac{1}{\mathrm{Re}} \boldsymbol{\nabla}^2 \boldsymbol{u}, \tag{3b}$$

The nondimensionalization factors are the chord length $c$ for distances and $c/U_\infty$ for time. Moreover we have $s = 3c$. In this framework, we have

$$\frac{\mathrm{Re}_\Gamma}{\mathrm{Re}_c} = \frac{\Gamma}{2\pi}. \tag{4}$$

The calculations are performed using the incompressible spectral element solver Nek5000.

## IV. Bénard–von Kármán vortex street

The wake of a NACA0012 wing at low incidence and low Reynolds number exhibits various forms of wakes just behind the wing body. In this section, we compare the wakes generated by the wing body (far from the tip) with the Floquet stability analysis and the numerical observations performed in [24]. For more general studies, one can also look at [25–27]. Furthermore, we describe the influence of the finiteness of the wing on this wake. The nature of instabilities is described as dependent on the angle of attack and Reynolds number. For small angles of attack and low Reynolds numbers, 2D instabilities are observed, while for large angles of attack and higher Reynolds numbers, 3D instabilities occur.

Table 1 lists the type of 2D structures obtained by the present simulations, depending on the Reynolds number and the angle of attack. The same structures highlighted in [24, fig. 7] are also observed, as well as the $\alpha_{3D}$ transition angle, that marks the threshold between the 2D and 3D structures. The alternative vortex shedding mode (AVS) is very similar to the classical Bénard von Kármán wake. The only difference lies in the slight downward deviation of the mean flow,

**Table 1 The different regimes of 2D wakes obtained as a function of the Reynolds number and angle of attack. AVS : Alternative vortex shedding; LAVP : Leftward alternative vortex pair; NAVP : Neutral alternative vortex pair.**

| Re \ AoA | 5° | 8° | 10° |
|---|---|---|---|
| 3000 | AVS* | AVS* | NAVP† |
| 4000 | AVS* | LAVP† | NAVP† |
| 5000 | AVS* | NAVP† | NAVP† |
| 7500 | AVS† | | |
| 10000 | AVS† | | |

*2D wake; †3D wake

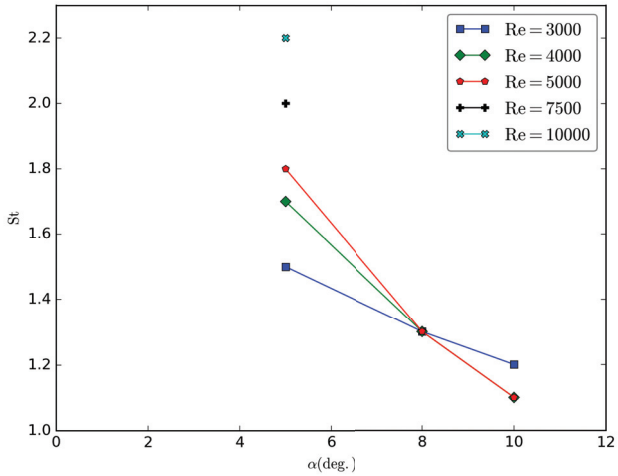


**Fig. 2 Strouhal number of vortex shedding behind the center of the wing, as a function of Reynolds number and angle of attack**

due to the non-zero angle of attack. The leftward alternative vortex pair mode (LAVP) exhibits successive vortex pairs, with the leading vortex having negative vorticity. This results in a downward deviation of the mean flow due to mutual induction between each vortex pair. In contrast, the neutral alternative vortex pair mode (NAVP) exhibits successive vortex pairs, with the leading vortex having positive vorticity. The upward velocity induced compensates for the natural downward motion, resulting in a horizontal motion of the mean flow. On fig. 2, we plotted the Strouhal number, defined by

$$St = \frac{fc}{U_\infty}, \tag{5}$$

with $f$ the shedding frequency, as a function of Reynolds number and angle of attack. The results are consistent with [24, fig. 6] for purely 2D wakes (see table 1), in particular the "Drop 1" bifurcation for Re = 3000 and 4000. Figure 3 also provides a slice of the spanwise vorticity profiles for the different flow regimes. We cannot observe the predicted bifurcations "Drop 2" for 2D regime transitions since the transition to 3D occurs before. The angle of attack of transition between the 2D and 3D regimes is of the form $\alpha = \mathrm{Re}^{-1/2}$ [24]. The 3D nature of the wake is visible in fig. 3 (c) and fig. 3 (e). Figure 4 shows the 3D structures obtained for the streamwise vorticity, which can be compared with [24, figs. 12 and 17].

All these comparisons to the literature allow us to conclude that the mesh we use around the wing is good enough. Moreover, we compared two meshes with different point densities to ensure its convergence.

A contour plot of the spanwise vorticity behind the wing is visible on fig. 5. Due to the presence of a wing tip in our study, the obtained instabilities are not independent of the spanwise direction. Near the wingtip, where the tip vortex rolls up, the vortex alley fades more quickly. In addition, the vortex shedding is not synchronized along the wing, and

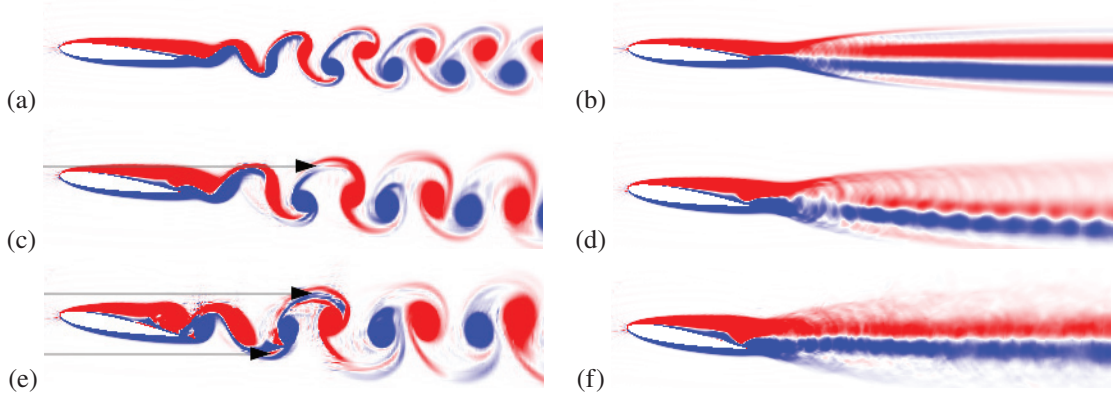


**Fig. 3 Slices of instantaneous (a,c,e) and time-averaged (b,d,f) spanwise vorticity profiles. (a,b) Alternative vortex shedding (AVS),** Re = 5000, $\alpha = 5°$ **; (c,d) Leftward alternative vortex pair (LAVP),** Re = 4000, $\alpha = 8°$ **; (e,f) Neutral alternative vortex pair (NAVP),** Re = 4000, $\alpha = 10°$**. 3D perturbations are visible in images (c) and (e), see arrows.**

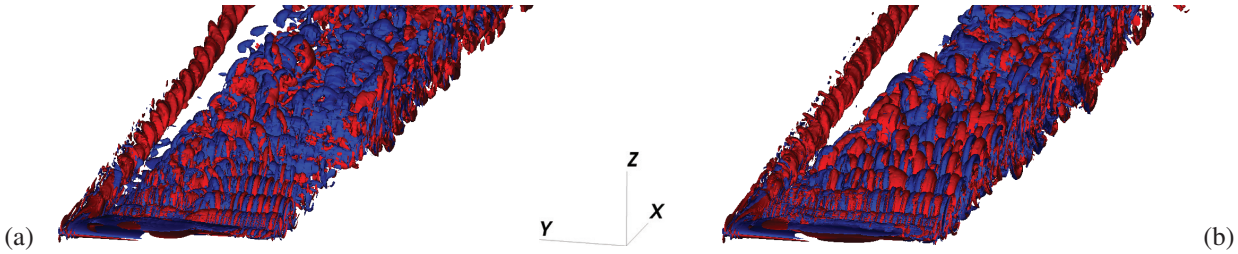


**Fig. 4 Streamwise vorticity coutour plot at** Re = 4000 **and (a)** $\alpha = 8°$ **; (b)** $\alpha = 10°$**.**

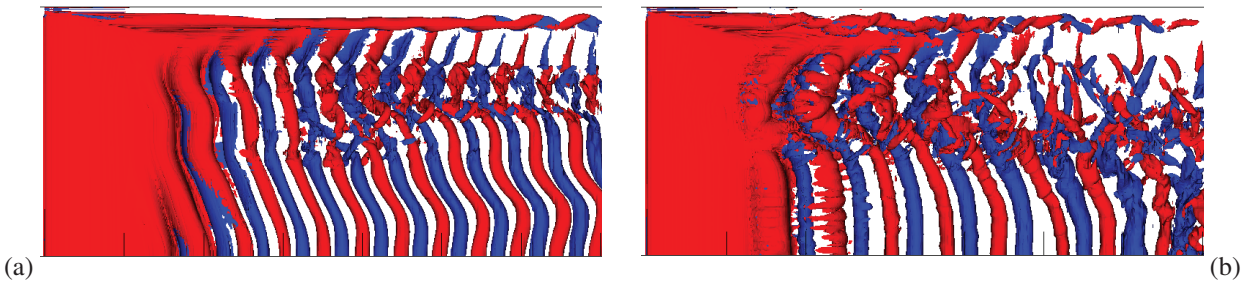


**Fig. 5 Top view of iso-values of spanwise vorticity at (a)** Re = 5000, $\alpha = 5°$ **; (b)** Re = 4000, $\alpha = 8°$**.**

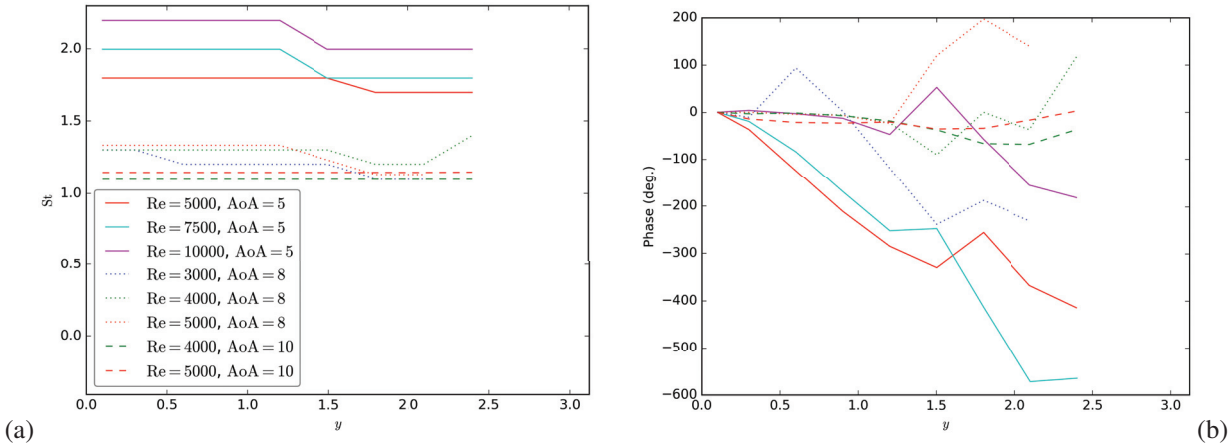


(a) (b)

**Fig. 6 (a) Strouhal number and (b) shedding phase shift relative to the wing center (in degrees), calculated at the trailing edge, as a function of Reynolds number and angle of attack.**

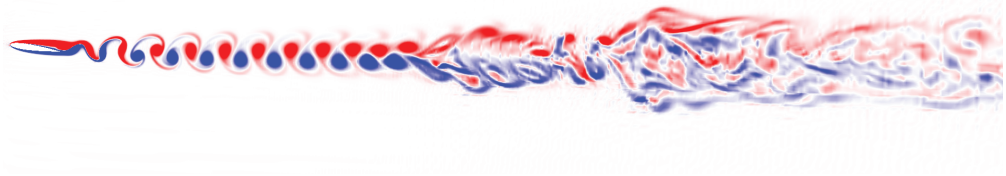

**Fig. 7 Slice of instantaneous spanwise vorticity profiles,** Re = 4000, $\alpha = 8°$**.**

the vorticity lines are therefore not parallel to the wing. On the other hand, the shedding frequency is very weakly dependent on the position along the wing, even though it appears to decrease slightly as one approaches the wing tip. Figure 6 shows the Strouhal number and the shedding phase shift relative to the wing center, calculated at the trailing edge, as a function of Reynolds number and angle of attack. The points closest to the wing tip do not exhibit noticeable oscillations, and the structures appearing at this level seem to result from an extension of the vortices in the inward direction. It appears that the higher the angle of attack, the less the frequency depends on the spanwise position behind the wing. Similarly, the phase difference along the wing is less important for a higher angle of attack. This can be explained in particular by the absence of frequency variation along the wing for an angle of attack of 10 degrees, except for Re = 3000, which closely resembles what is observed at $\alpha = 8$ degrees. For angles of attack of 5 and 8 degrees, there are two regions with two frequencies that are close but slightly different. Those two regions are found again in the phase curve, with two different slopes.

At a certain distance downstream of the wing (which depends on the parameters), the Von Kármán wake looses its coherent structure and becomes more turbulent (fig. 7).

## V. Wake vortex generation and mean flow properties

The tip vortex develops just behind the wing and then forms a vortex tube in the direction of the flow. It is perturbed by the Von Kármán vortex street right from its formation, as can be seen in fig. 4. The initial circulation and radius of the vortex as a function of angle of attack and Reynolds number is given in fig. 8. As expected, the initial value of the circulation mainly depends on the angle of attack, that is, on the lift. It should be noted that velocities are non-dimensionalized by the upstream fluid velocity. Thus, for the range of interest here, the circulation of the vortex is not proportional to the Reynolds number.

Furthermore, it was mentioned in section III that the distance between the vortex and the symmetry plane is expected to increase up to $b/2 = 0.44$. However, in practice, the average vortex (obtained by averaging snapshots at different times) deviates less than expected, as shown in fig. 9 (b). This can be explained by the proximity of the symmetry plane

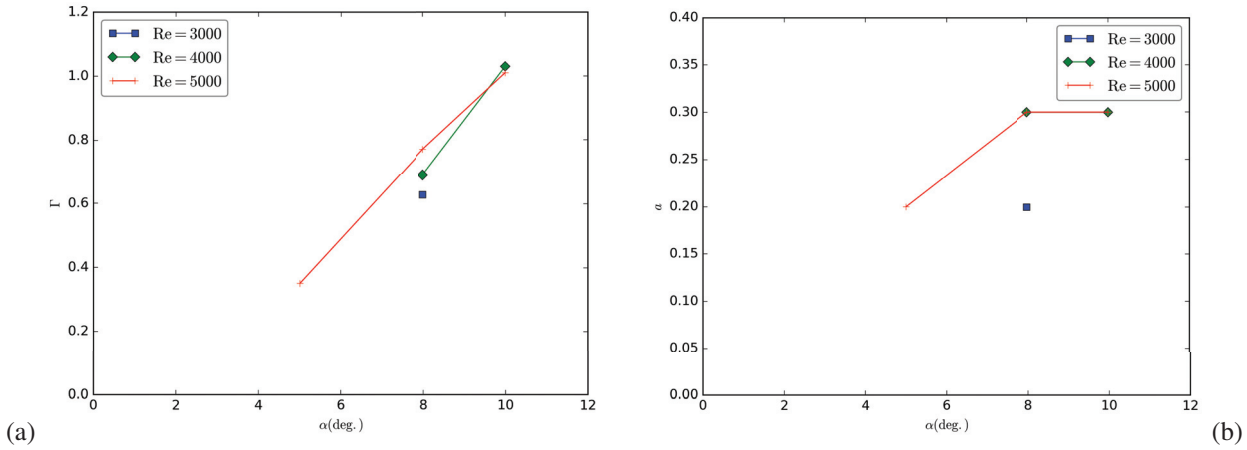


**Fig. 8 Initial circulation (a) and vortex radius (b) as a function of angle of attack.**

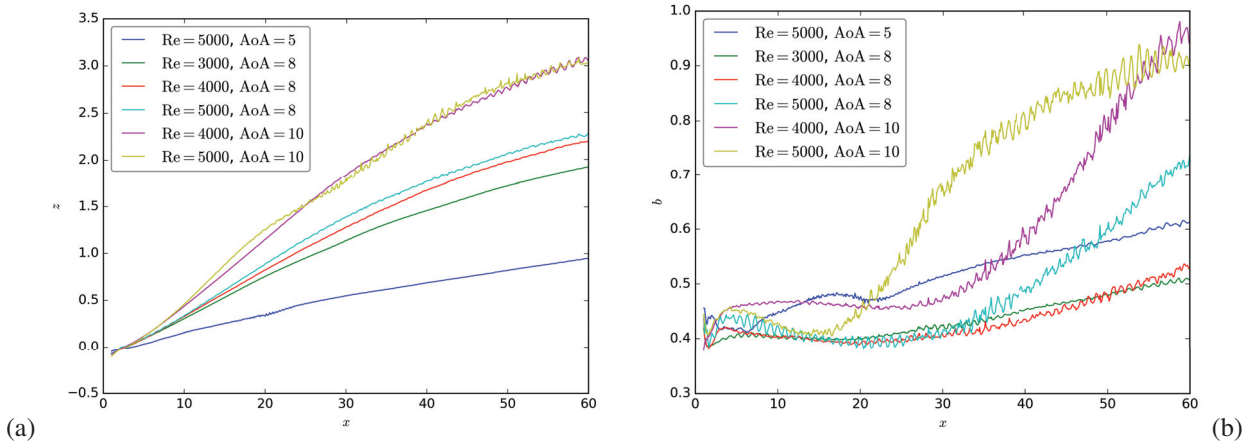


**Fig. 9 Evolution of (a) the altitude and (b) the separation of the wingtip vortices as a function of the downstream distance from the wing. It should be noted that the large separation values observed are due to the formation of vortex rings.**

and the early interaction of the vortex with its image, long before most of the wrapping is completed. Moreover, due to the symmetry, the altitude of the vortex increases by induction as it moves downstream of the wing (fig. 9 (a)). With this data, it is now possible to compute the circulation-based Reynolds number, that we present on fig. 10.

Figure 11 shows a cross-section of the streamwise vorticity of the mean flow at several distances downstream of the wing. It shows the formation of the tip vortex (to the right of (a-b-c)) and the Von Kármán wake (in the center of (a-b-c)), the degeneration of the Von Kármán wake and its influence on the vortex (c-d), and then their separation once the vortex is rolled up and rises (d-e).

## VI. Wake vortex instabilities

First, an iso-value of streamwise vorticity is plotted on fig. 12 to get an idea of the shape and position of the wake vortex. Two main types of instabilities appear in our study, and only a limited number of cases (for instance (a) and (b)) seams to reach a longwave instability. The others show another instability with a shorter wavelength, for higher Reynolds numbers or larger angles of attack (for instance (c) and (d)). Table 2 summarizes the instabilities that develop as a function of angle of attack and Reynolds number. Note that these two instabilities affect the position of the vortex. If we look again at fig. 10, we can see that the separation between these two cases corresponds to crossing a threshold in the circulation-based Reynolds number values.

In this section, we first consider the velocity field resulting from the difference between the mean field and a snapshot,

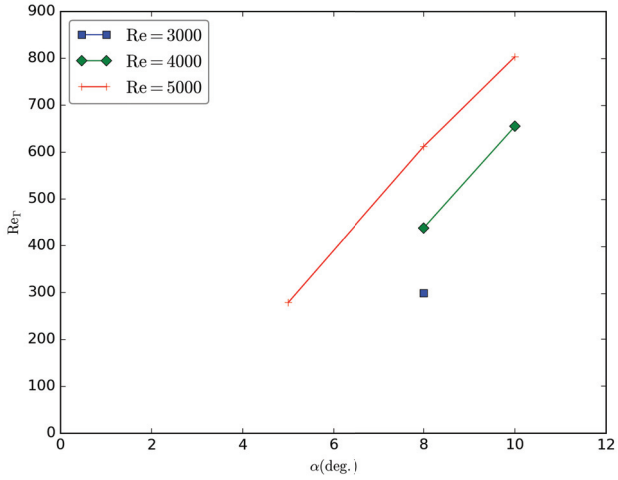


**Fig. 10** $\mathrm{Re}_\Gamma$ **as a function of** $\mathrm{Re}_c$ **and** $\alpha$

**Table 2 The different regimes of wake vortex instability obtained as a function of the Reynolds number and angle of attack. LW: longer wavelength instability; SW: shorter wavelength instability.**

| Re \ AoA | 5° | 8° | 10° |
|---|---|---|---|
| 3000 | | LW | SW |
| 4000 | | SW | SW |
| 5000 | LW | SW | SW |
| 7500 | SW | | |
| 10000 | SW | | |

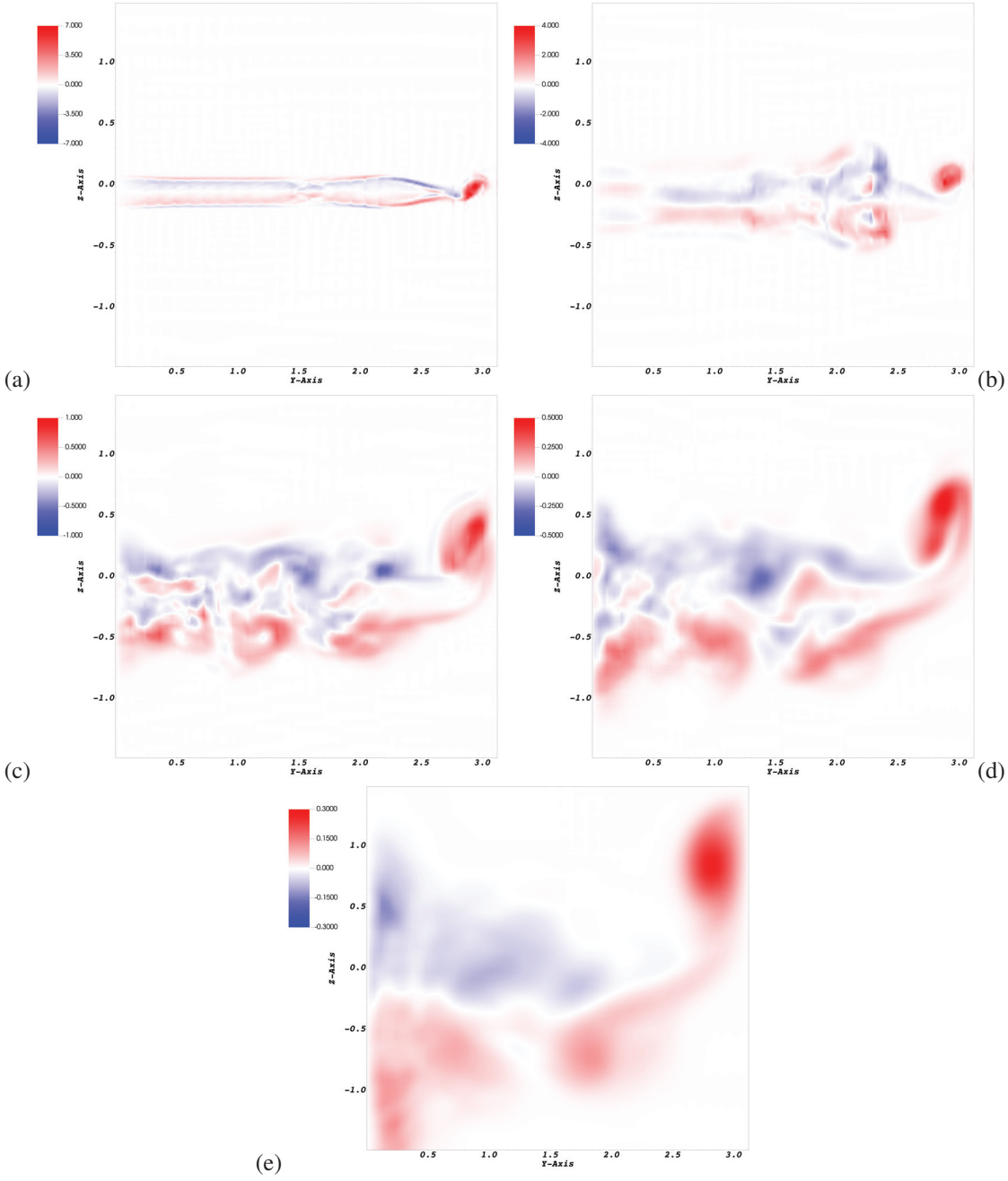


**Fig. 11 Streamwise vorticity profile of the mean flow at several distances downstream of the wing: (a)** 0.5**, (b)** 5**, (c)** 15**, (d)** 25**, (e)** 50 **for** Re = 5000 **and** $\alpha = 5°$**. The colorbar limits are not the same for the first image and the following ones.**

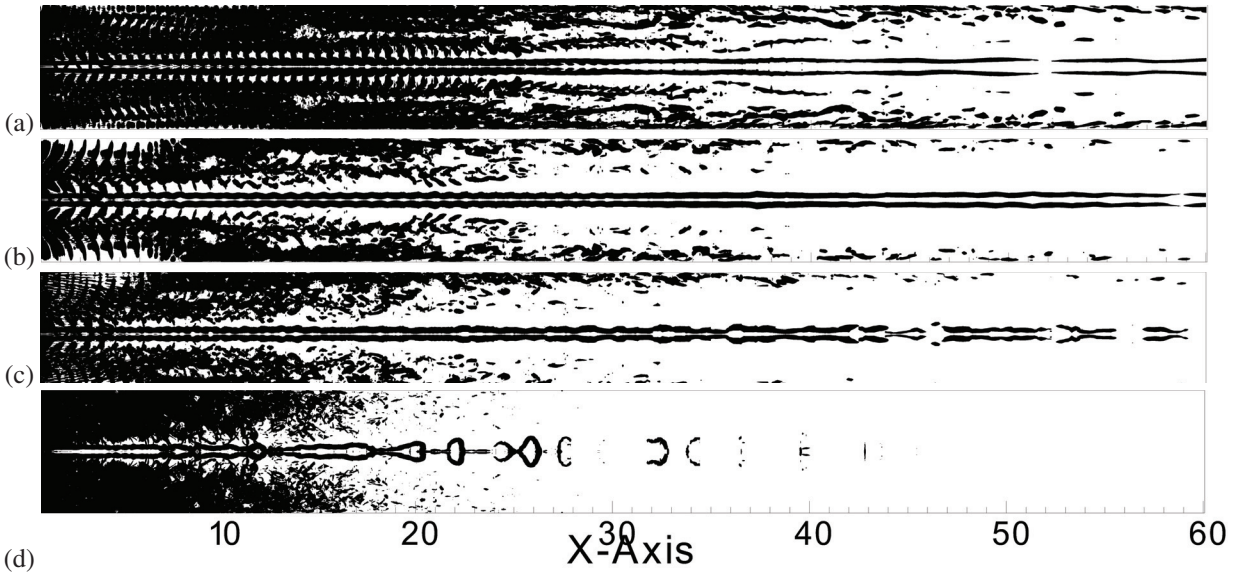


**Fig. 12 Iso-contour of the streamwise vorticity. A mirror effect has been applied at the symmetry plane level. (a)** Re = 5000**,** $\alpha = 5°$**; (b)** Re = 3000**,** $\alpha = 8°$**; (c)** Re = 4000**,** $\alpha = 8°$**; (d)** Re = 5000**,** $\alpha = 10°$**.**

considered as a perturbation of the mean field. We analyze the deviation of the vortex position by searching for the frequencies of its movements, as long as they are defined. On the other hand, we use a Proper Orthogonal Decomposition (POD) to identify the main modes of the flow. This method allows to find an orthogonal basis of the vector space generated by snapshots of perturbations in the flow. The average of all these snapshots, referred to as the base flow, is calculated, and a spectral analysis of perturbations around this mean is performed (but not on the Fourier basis). The resulting vectors are called modes and are sorted by decreasing energy, meaning that the first modes correspond to the largest eigenvalues of the correlation matrix. This decomposition is optimal in the sense that, for a given number of POD modes, the projection onto the subspace generated by these modes contains the highest possible amount of kinetic energy.

### A. Longwave instability

We first study the occurrence of this instability through the case of Re = 3000 and $\alpha = 8°$. Figure 13 shows the isocontours of the streamwise vorticity for a perturbation field around the mean flow. Three distinct regions can be identified. The first zone is located within 10 chord lengths downstream of the wing. In this region, the interaction between the wing vortex and the Von Kármán wake structures causes the core of the vortex to move. This can be observed in fig. 14, which displays a cross-section of the perturbation streamwise vorticity at the vortex core. The second zone is between 10 and 30 chord lengths behind the wing. At this location, the vortex still retains the perturbation from the Von Kármán wake, but another perturbation with a much larger wavelength begins to form. Figures 15 and 16 display the perturbations due to this small and large wavelength. Finally, at more than 30 chord lengths downstream of the wing, the tip vortex is mostly free from the small wavelength perturbation, and only the movement of the core with the large wavelength remains, which can be seen in more detail in fig. 17. This division of the wake into three parts and the different wavelengths can also be identified through Proper Orthogonal Decomposition (POD) analysis. In particular, mode 1 is represented in fig. 18.

We now compare the previous case to the case where Re = 5000 and $\alpha = 5°$. We can see from fig. 19 that the vorticity of the perturbation varies little between the two cases. The initial perturbations ($x \leqslant 10$) are also very similar. However, it can be seen in fig. 20 that there is a perturbation of the form $m = 2$ in the section $10 \leqslant x \leqslant 30$, which was not visible in the first case. This mode then fades away, and starting from $x = 30$, we can observe the long-wavelength mode identified earlier, as shown in fig. 21. This time, POD mode 2 is the first to capture these behaviors (see fig. 22).

Furthermore, another difference is observed in the evolution of the Von Kármán wake. The coherent structures formed near the wing tend to degenerate as usual, but in addition, they have a tendency to oscillate at the same large wavelength near the wingtip vortex. This can be seen in the perturbation plot and in the POD modes in fig. 22.

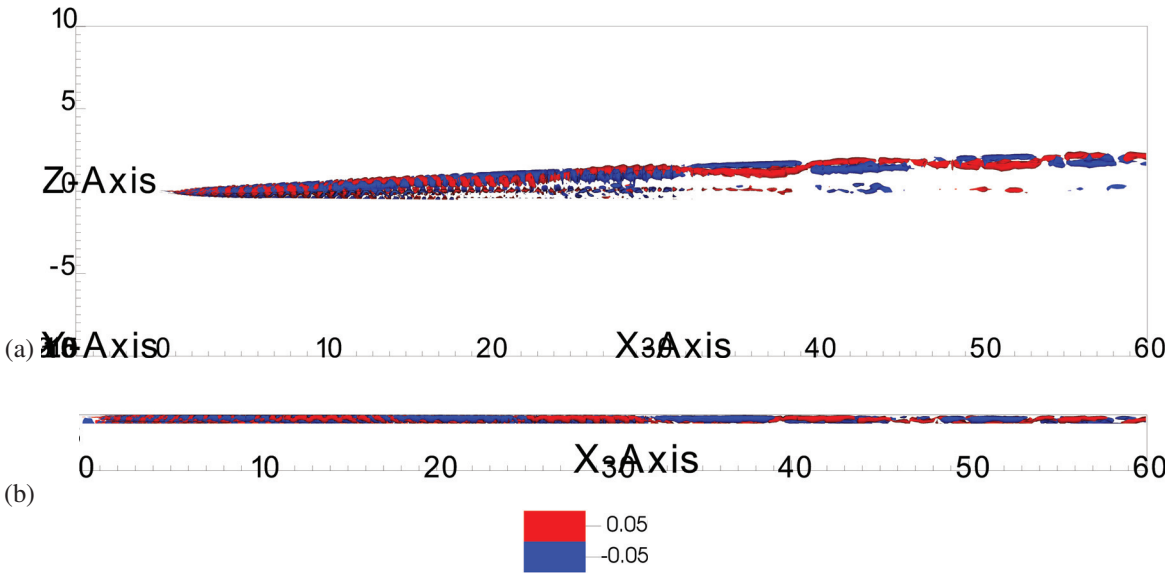


**Fig. 13 (a) Lateral and (b) top view of perturbation streamwise vorticity contour plot for** Re = 3000 **and** $\alpha = 8°$**. Only the structures near the mean vortex are represented.**

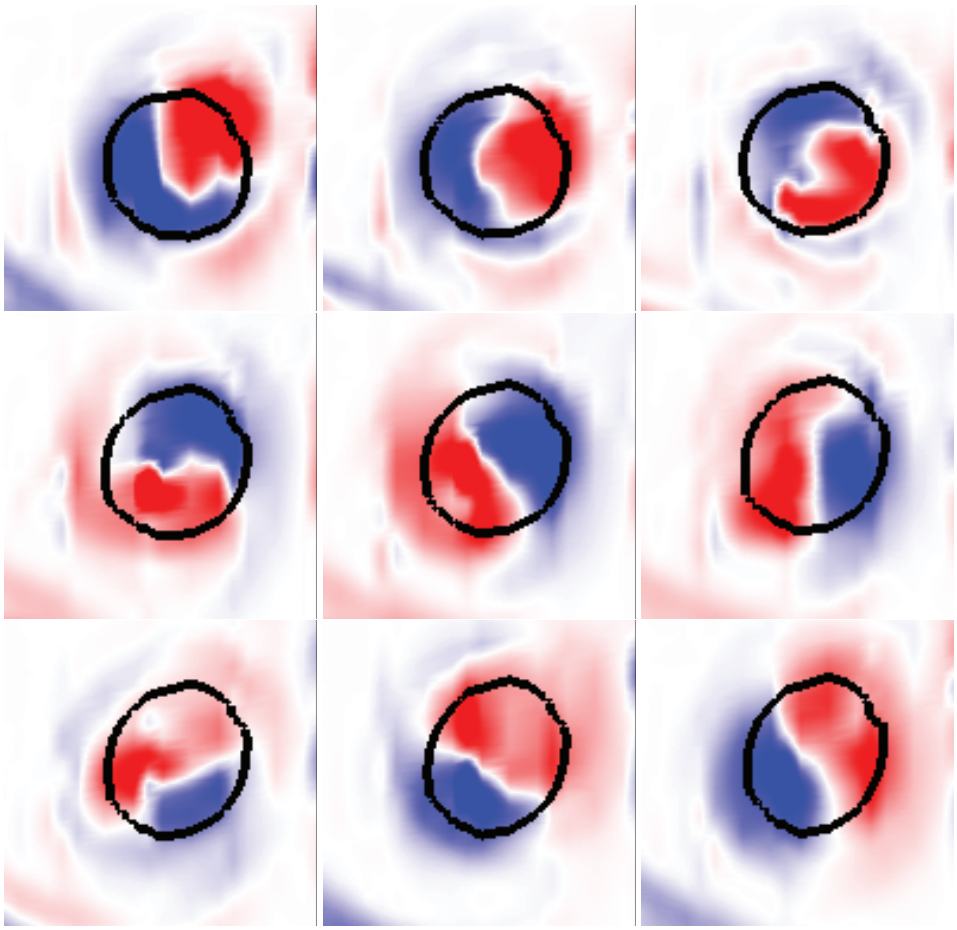

**Fig. 14 Transverse cross-section of the streamwise vorticity perturbation field (shown in color). The black line represents the contour of the streamwise vorticity of the mean field.** $x = 3$**,** 3.1**,** 3.2**,** 3.3**,** 3.4**,** 3.5**,** 3.6**,** 3.7 **and** 3.8**.** Re = 3000 **and** $\alpha = 8°$**.**

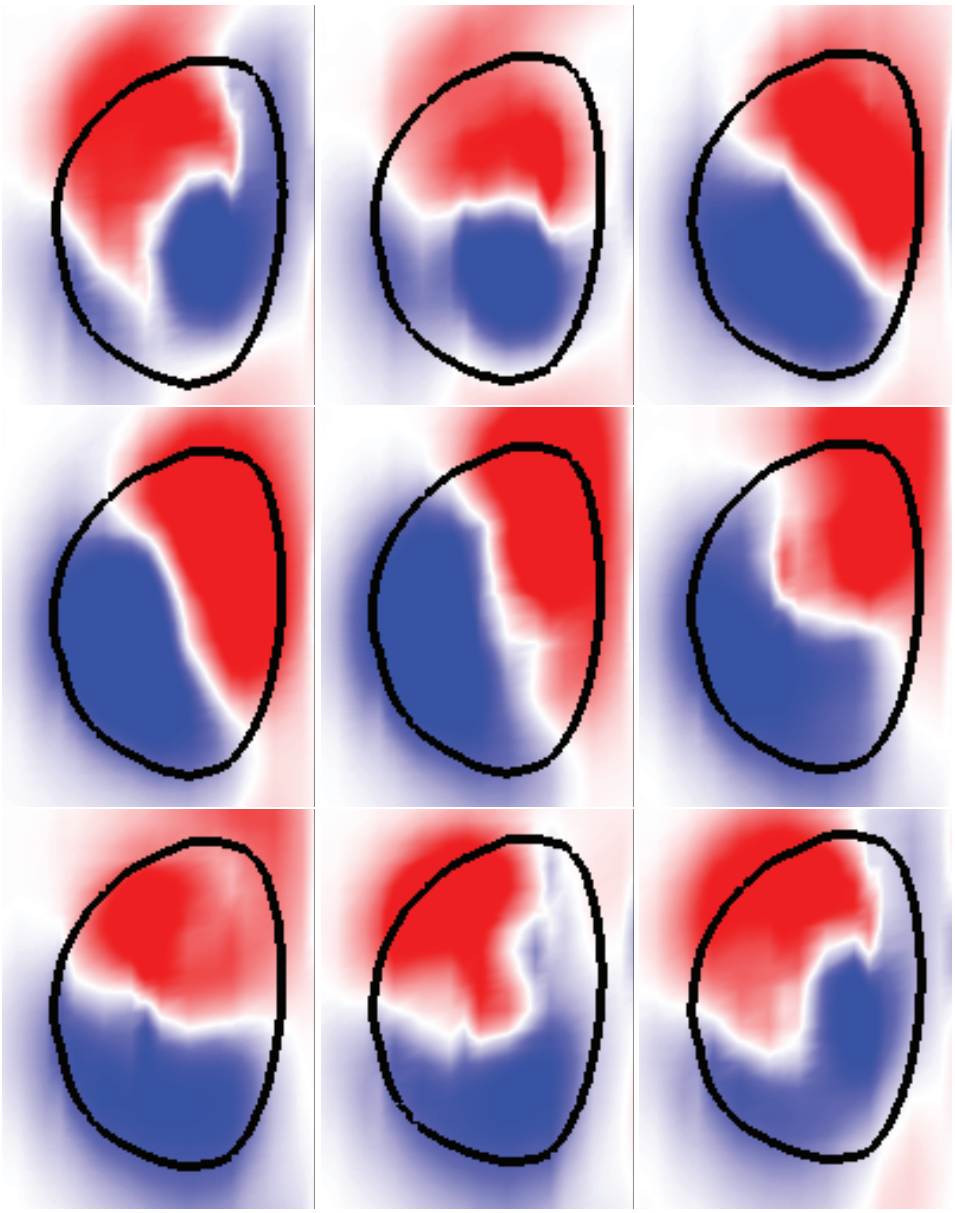

**Fig. 15 Transverse cross-section of the streamwise vorticity perturbation field (shown in color). The black line represents the contour of the streamwise vorticity of the mean field.** $x$ = 12**,** 12.1**,** 12.2**,** 12.3**,** 12.4**,** 12.5**,** 12.6**,** 12.7 **and** 12.8**.** Re = 3000 **and** $\alpha = 8°$**.**

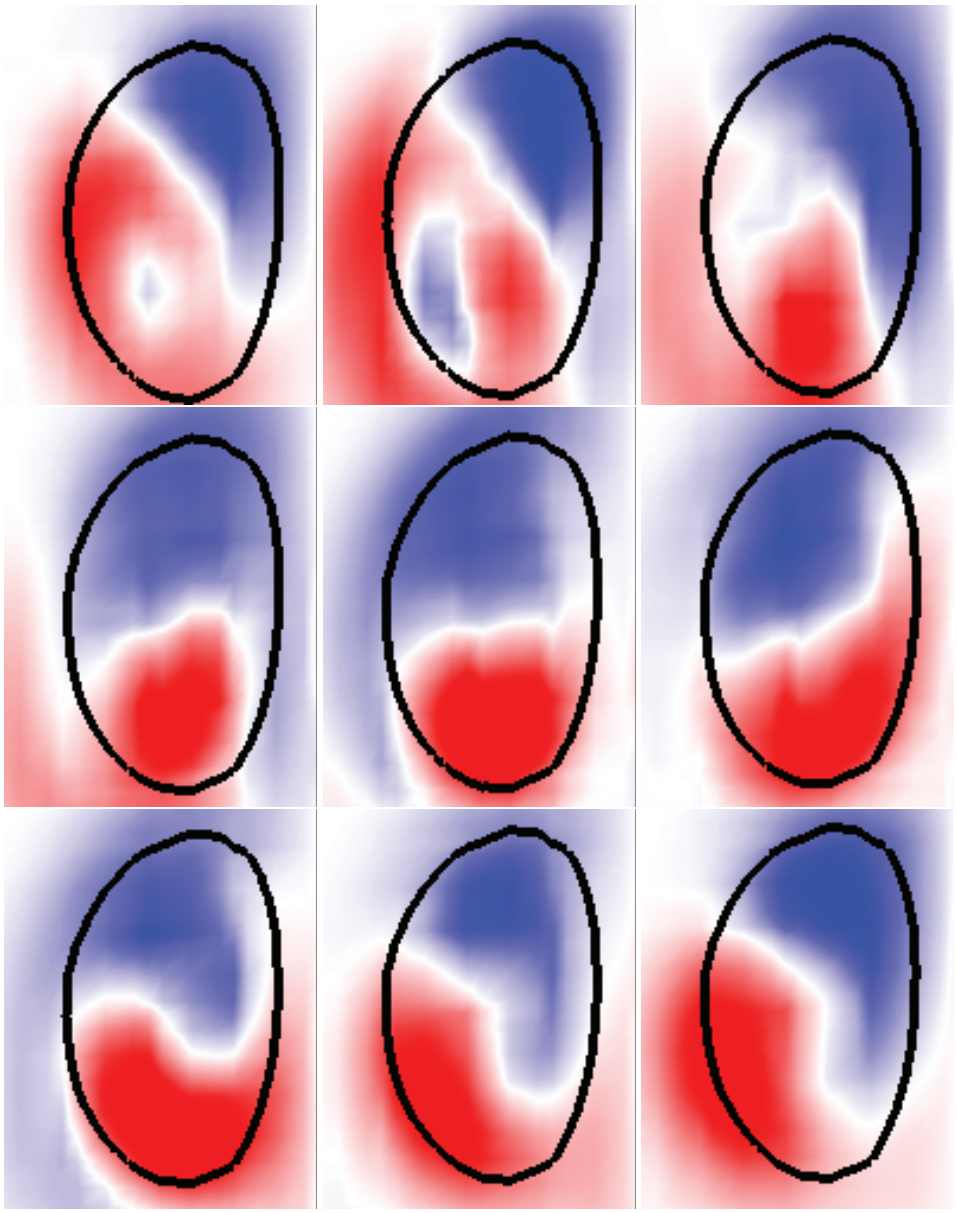

**Fig. 16 Transverse cross-section of the streamwise vorticity perturbation field (shown in color). The black line represents the contour of the streamwise vorticity of the mean field.** $x$ = 20**,** 20.1**,** 20.2**,** 20.3**,** 20.4**,** 20.5**,** 20.6**,** 20.7 **and** 20.8**.** Re = 3000 **and** $\alpha = 8°$**.**

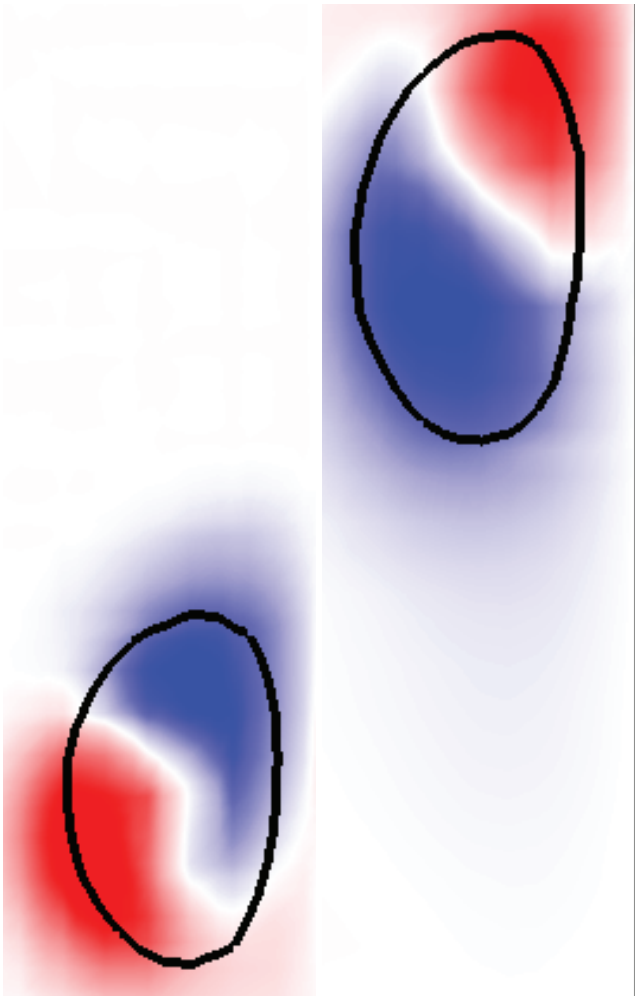

**Fig. 17 Transverse cross-section of the streamwise vorticity perturbation field (shown in color). The black line represents the contour of the streamwise vorticity of the mean field.** $x = 37$ **and** $43$**.** $\mathrm{Re} = 3000$ **and** $\alpha = 8°$**.**

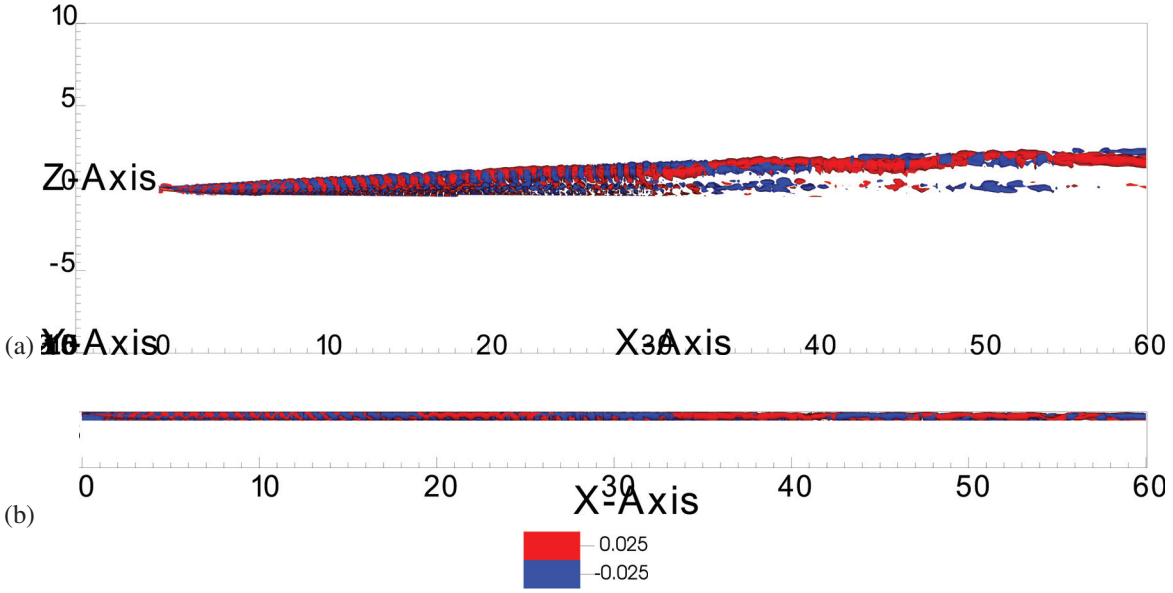


**Fig. 18 (a) Lateral and (b) top view of the streamwise vorticity contour plot of the first POD mode calculated from 80 snapshots for Re = 3000 and $\alpha = 8°$. Only the structures near the mean vortex are represented.**

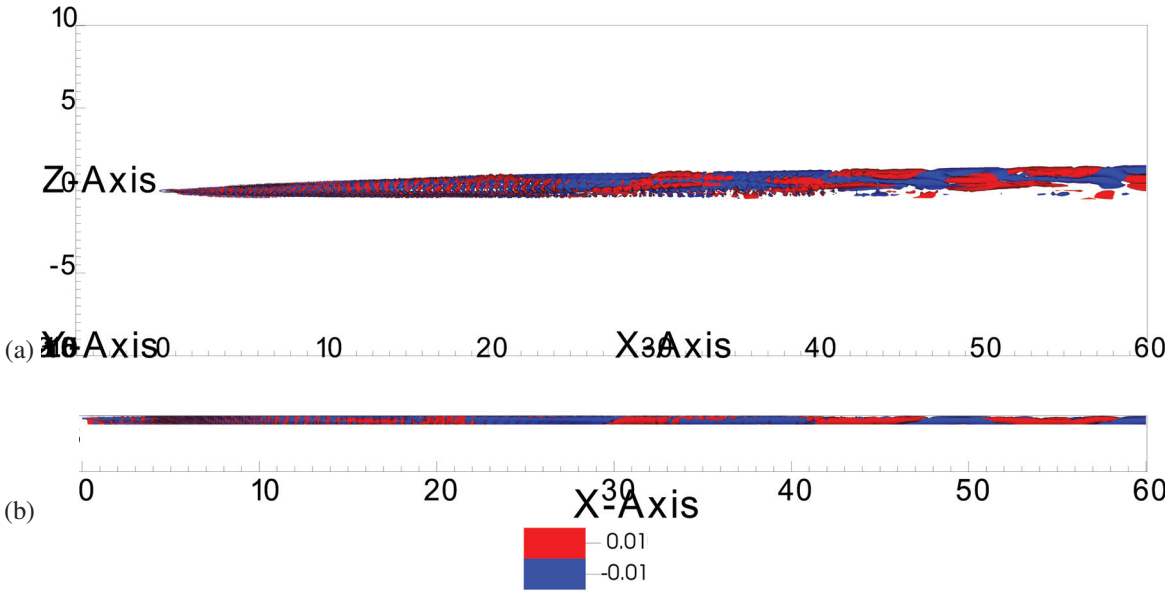


**Fig. 19 (a) Lateral and (b) top view of perturbation streamwise vorticity contour plot for Re = 5000 and $\alpha = 5°$. Only the structures near the mean vortex are represented.**

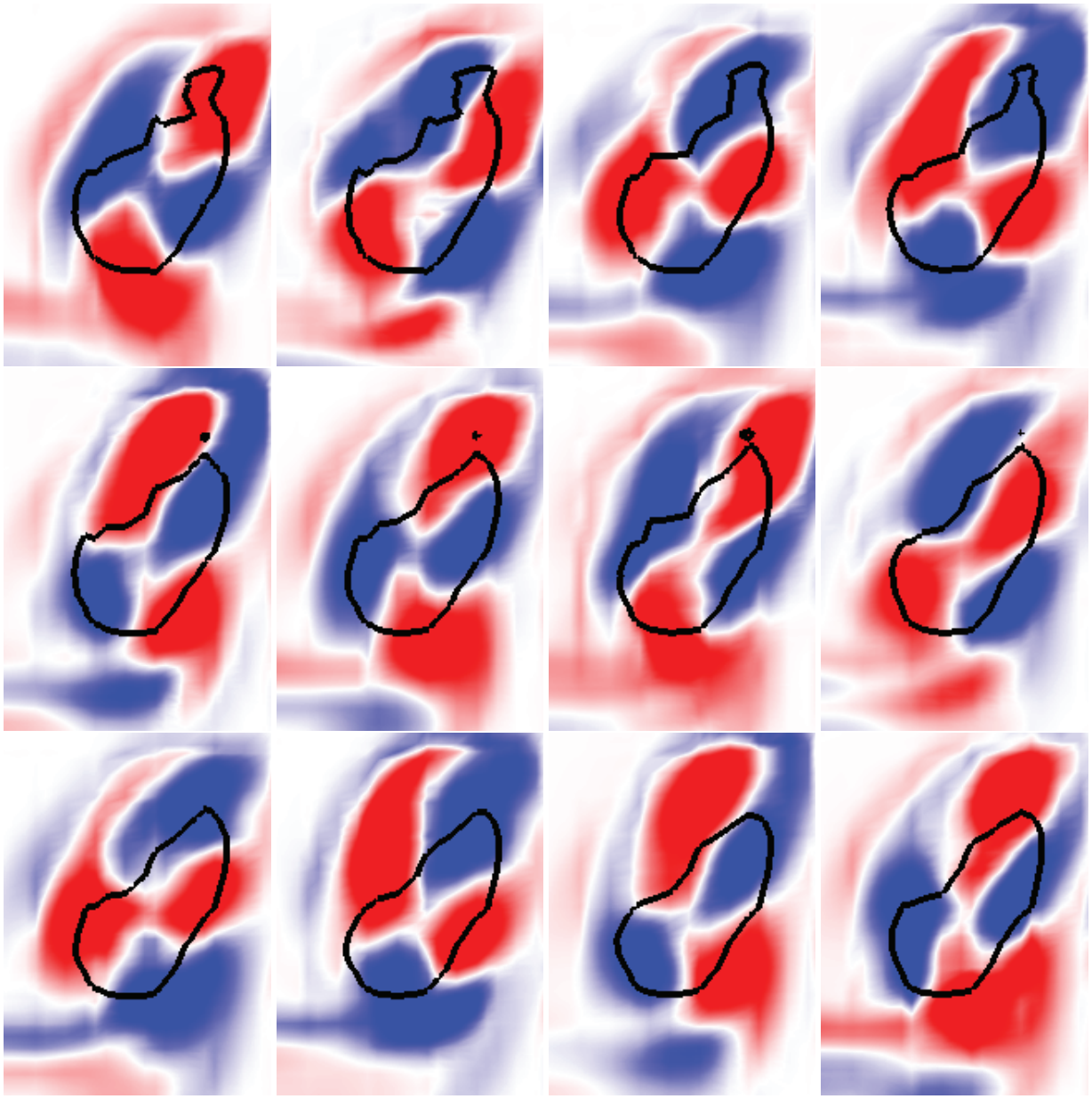

**Fig. 20 Transverse cross-section of the streamwise vorticity perturbation field (shown in color). The black line represents the contour of the streamwise vorticity of the mean field.** $x$ = 12.1**,** 12.2**,** 12.3**,** 12.4**,** 12.5**,** 12.6**,** 12.7**,** 12.8**,** 12.9**,** 13**,** 13.1 **and** 13.2**.** Re = 5000 **and** $\alpha = 5°$**.**

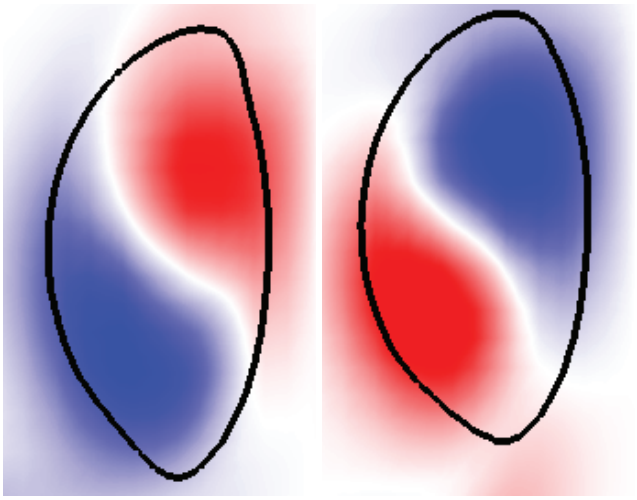

**Fig. 21 Transverse cross-section of the streamwise vorticity perturbation field (shown in color). The black line represents the contour of the streamwise vorticity of the mean field.** $x = 46.5$ **and** $49.5$**.** Re $= 5000$ **and** $\alpha = 5°$**.**

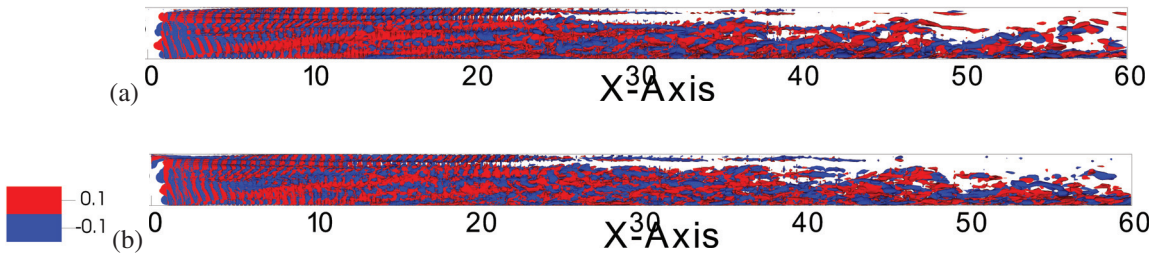


**Fig. 22 Top view of (a) perturbation streamwise vorticity contour plot and (b) the second POD mode calculated from** $80$ **snapshots, for** Re $= 5000$ **and** $\alpha = 5°$**.**

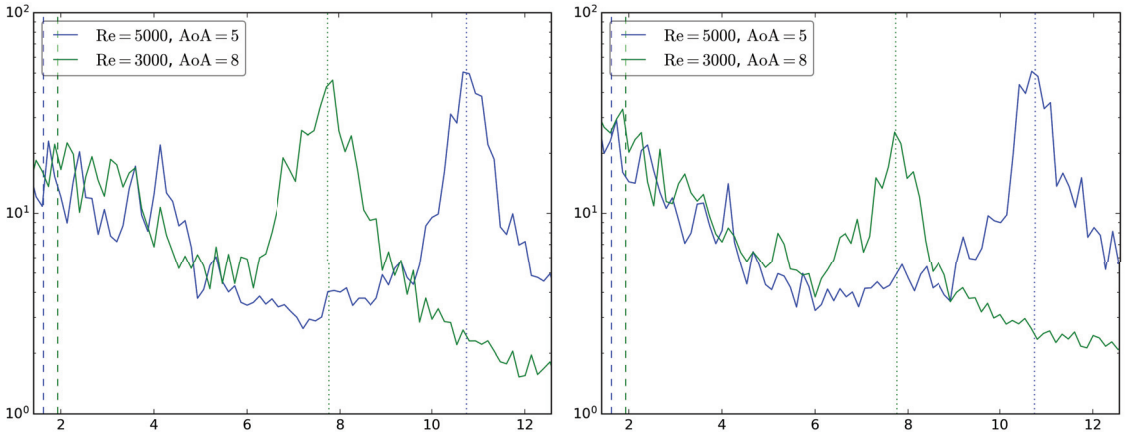


**Fig. 23 Amplitude of the vortex displacement as a function of the streamwise wavenumber of the (a) horizontal and (b) vertical vortex displacement around its mean position. The dashed lines indicates the Crow frequency and the dotted lines the Von Kármán frequency.**

The mean Fourier spectrum of the displacement of the vortex center with respect to its mean is shown in fig. 23. While the presence of a large wavelength ($k \leqslant 4$) appears to be evident, it does not seem to be well determined. However, the influence of the Von Kármán wake is very visible ($7 \leqslant k \leqslant 12$).

### B. Shorter-wavelength instability

We now aim to investigate the occurrence of shorter-wavelength perturbations in the wingtip vortex. We study this case using the flow obtained for Re = 4000 and $\alpha = 8°$. We focus on the vortex motion before it breaks apart, which appears to occur at $x \simeq 46$. Three distinct zones can be identified in the perturbation vorticity contour plot presented in fig. 24. Firstly, the vortex is perturbed, similar to the previous case, by the Von Kármán vortex street. However, in this case, the way the vortex is perturbed does not appear to exhibit a truly periodic motion, as shown in fig. 25. Furthermore, the intensity of the perturbation appears to be much weaker: the vorticity of the perturbation is an order of magnitude smaller. Then, a perturbation of larger wavelength but smaller than in the previous section emerges, still influenced by the initial perturbation, as depicted in fig. 26. Finally, the vortex follows oscillatory motion at this latter wavelength only, as observed in fig. 27, and may subsequently break and form vortex rings.

The mean Fourier spectrum of the displacement of the vortex center with respect to its mean is shown in fig. 28. In contrast to the previous case, it does not seem possible to observe any influence of the Von Kármán wake on these spectra. However, the wavenumbers associated with the larger wavelengths, but still smaller than in the previous case ($k \leqslant 5$) exhibit significant energy content. The comparison of the curves from the two separate cases clearly indicates that different phenomena occur.

## VII. Conclusion

We conducted a numerical study at Reynolds numbers between 3000 and 10 000 and moderate angle of attack (between 5 and 10 degrees) to investigate the occurrence of wake instabilities behind a slotted wing setup.

First, we focused on the von Kármán wake. We observed the various 2D and 3D regimes that have been reported in the literature. We noticed an influence of the wing's finiteness, manifested by slight modifications in the shedding frequency and a phase shift of the vortices. Close to the wingtip vortex, the von Kármán wake appears to disappear.

Next, we examined the wingtip vortex and the instabilities that develop in its vicinity. We identified two regimes, separated by a threshold Reynolds number based on circulation. These regimes differ in their response to the von Kármán wake and the wavelength of the instability downstream of the wing. For lower Reynolds numbers, the wingtip vortex strongly interacts with the von Kármán wake, and a large-wavelength instability develops in terms of its position. For higher Reynolds numbers, the wingtip vortex shows a weaker interaction with the von Kármán wake, and a smaller-wavelength instability emerges in terms of its position. This can lead to the formation of vortex rings. However, this instability is not considered a small-wavelength instability in the Widnall sense. For these two regimes,

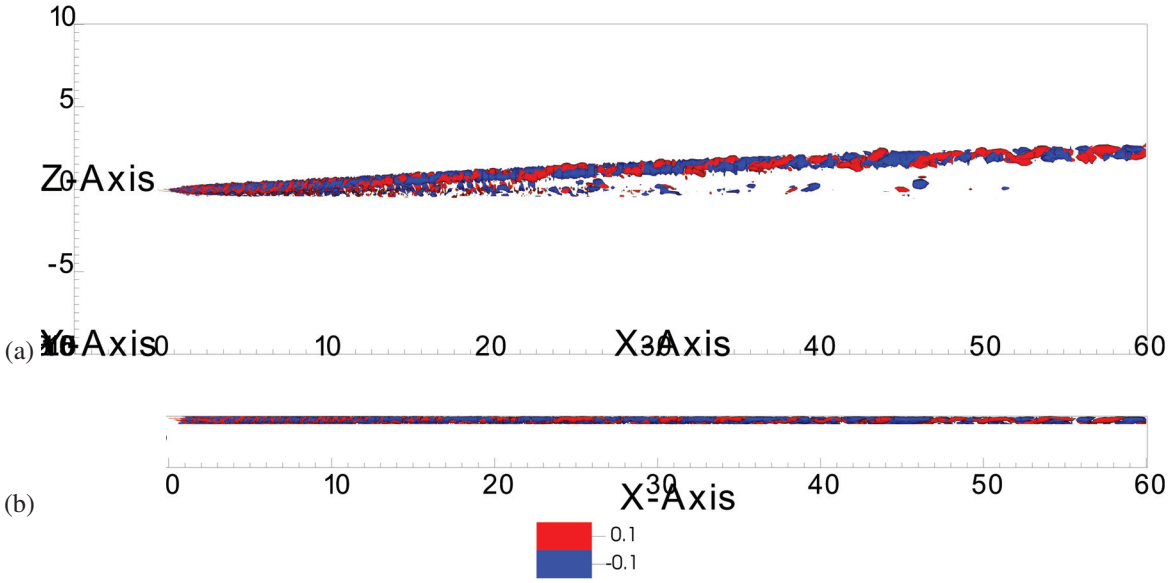


**Fig. 24 (a) Lateral and (b) top view of perturbation streamwise vorticity contour plot for** Re = 4000 **and** $\alpha = 8°$**. Only the structures near the mean vortex are represented.**

the wavelength obtained is quite variable.

Two spectral analyses have been conducted. The first one is a POD analysis that highlights the observed behaviors of the perturbation. The second one is a Fourier analysis of the position of the wingtip vortex as a function of the downstream distance from the wing. It helps to understand the difference in the wingtip vortex's response to the von Kármán wake and the diversity of wavelengths of the subsequent instabilities.

## References

[1] Unterstrasser, S., and Görsch, N., "Aircraft-type dependency of contrail evolution," *Journal of Geophysical Research: Atmospheres*, Vol. 119, No. 24, 2014, pp. 14,015–14,027.

[2] Saulgeot, P., Brion, V., Bonne, N., Dormy, E., and Jacquin, L., "Effects of atmospheric stratification and jet position on the properties of early aircraft contrails," , Mar. 2023. Preprint.

[3] Crow, S. C., "Stability theory for a pair of trailing vortices," *AIAA Journal*, Vol. 8, No. 12, 1970, pp. 2172–2179.

[4] Tsai, C.-Y., and Widnall, S. E., "The stability of short waves on a straight vortex filament in a weak externally imposed strain field," *Journal of Fluid Mechanics*, Vol. 73, No. 4, 1976, p. 721–733.

[5] Dee, F., and Nicholas, O., "Flight measurements of wing-tip vortex motion near the ground," *Aeronautical Research Council Current Papers*, , No. 1065, 1968.

[6] Scorer, R. S., and Davenport, L. J., "Contrails and aircraft downwash," *Journal of Fluid Mechanics*, Vol. 43, No. 3, 1970, p. 451–464.

[7] Eliason, B., Gartshore, I., and Parkinson, G., "Wind tunnel investigation of Crow instability," *Journal of Aircraft*, Vol. 12, No. 12, 1975, pp. 985–988.

[8] Leweke, T., and Williamson, C., "Cooperative elliptic instability of a vortex pair," *Journal of Fluid Mechanics*, Vol. 360, No. 85, 1998, p. 119.

[9] Leweke, T., and Williamson, C. H. K., "Experiments on long-wavelength instability and reconnection of a vortex pair," *Physics of Fluids*, Vol. 23, No. 2, 2011, p. 024101.

[10] Crow, S. C., and Bate, E. R., "Lifespan of trailing vortices in a turbulent atmosphere," *Journal of Aircraft*, Vol. 13, No. 7, 1976, pp. 476–482.

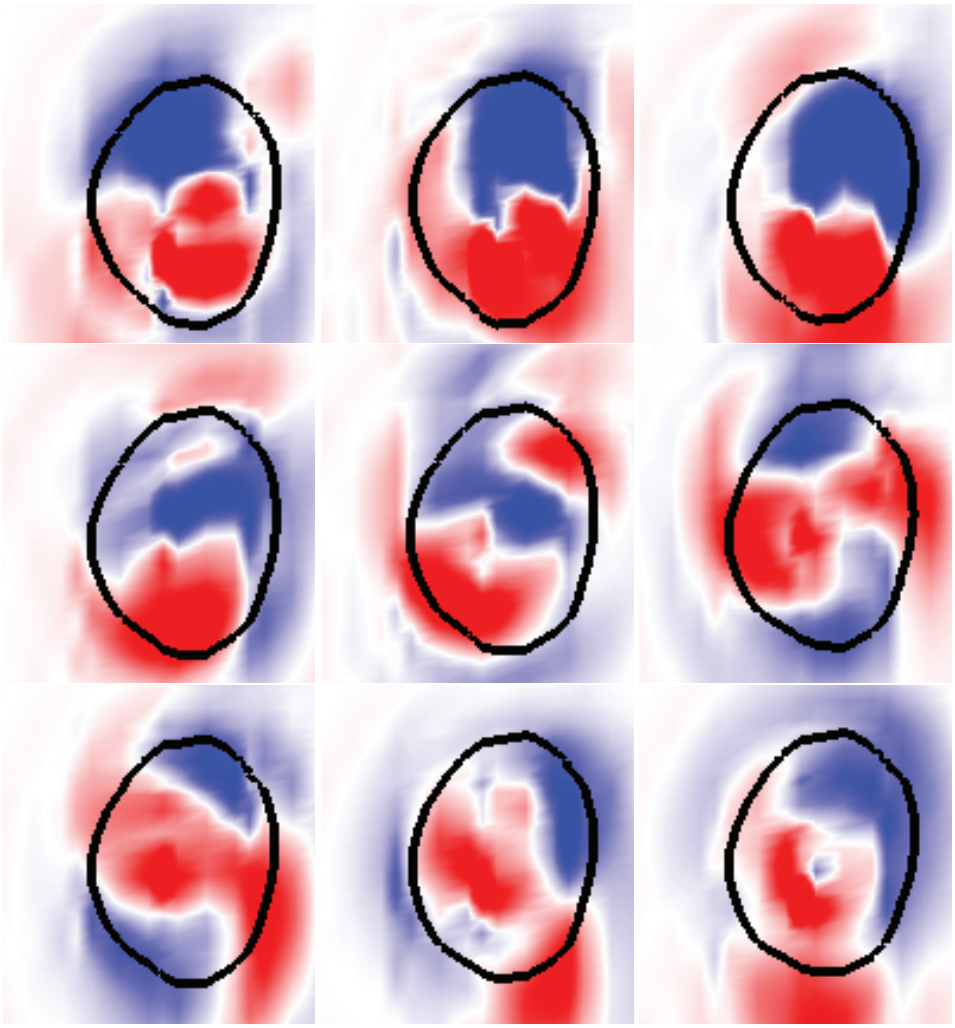

**Fig. 25 Transverse cross-section of the streamwise vorticity perturbation field (shown in color). The black line represents the contour of the streamwise vorticity of the mean field.** $x$ = 7**,** 7.1**,** 7.2**,** 7.3**,** 7.4**,** 7.5**,** 7.6**,** 7.7 **and** 7.8**.** Re = 4000 **and** $\alpha = 8°$**.**

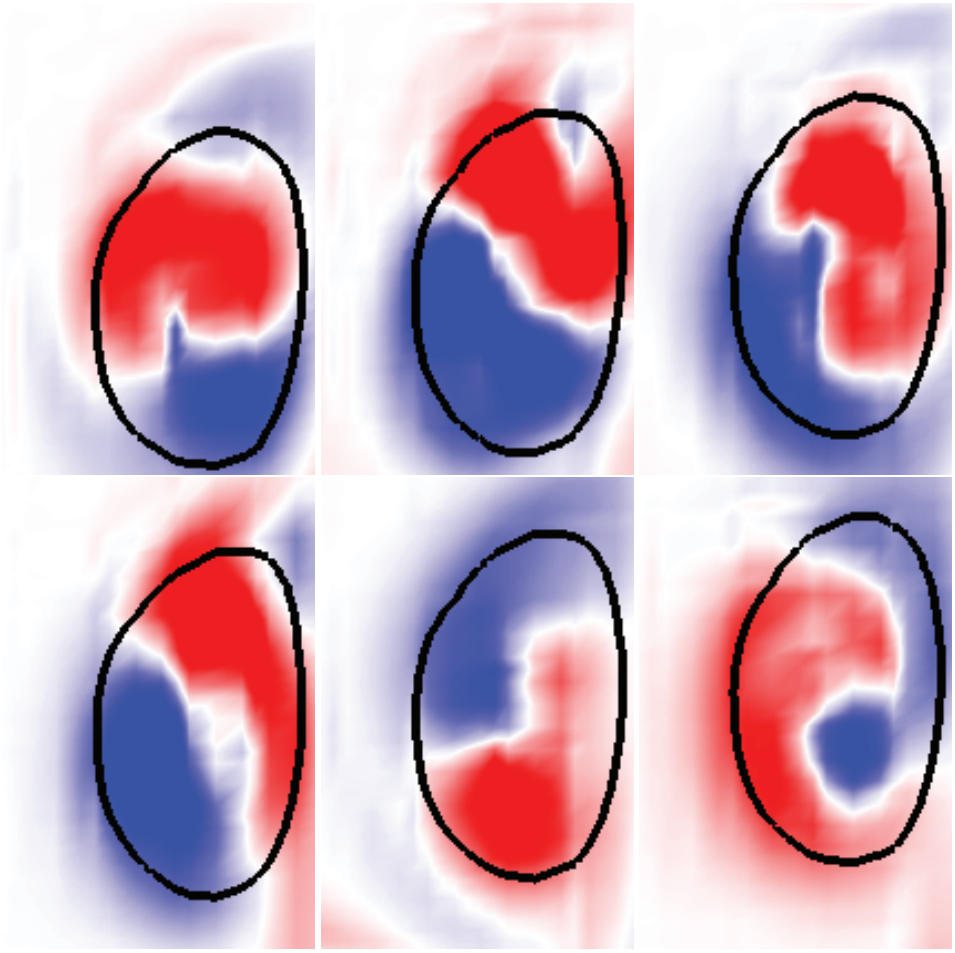

**Fig. 26 Transverse cross-section of the streamwise vorticity perturbation field (shown in color). The black line represents the contour of the streamwise vorticity of the mean field.** $x$ = 15**,** 15.5**,** 16**,** 16.5**,** 17 **and** 17.5**.** Re = 4000 **and** $\alpha = 8°$**.**

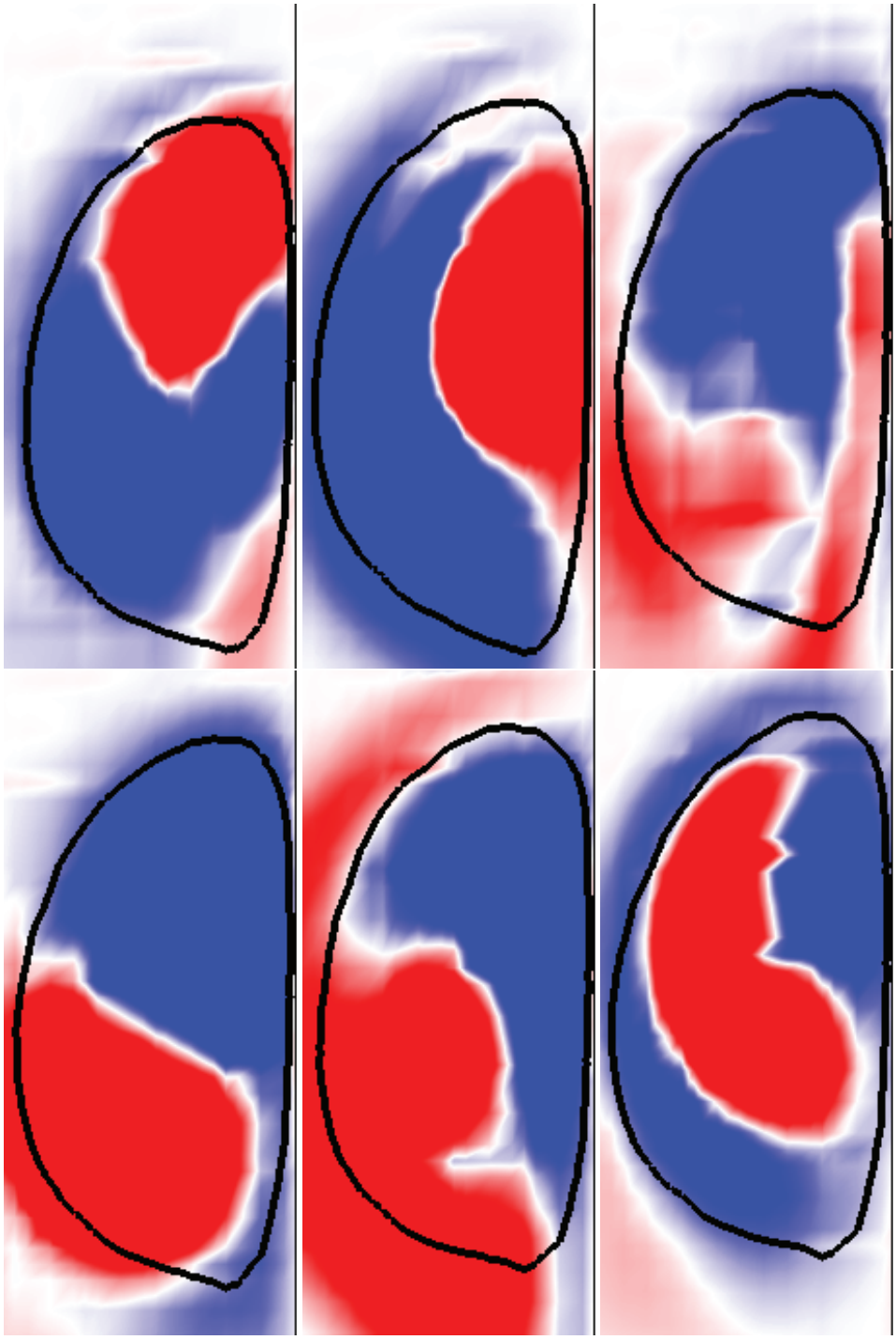

**Fig. 27 Transverse cross-section of the streamwise vorticity perturbation field (shown in color). The black line represents the contour of the streamwise vorticity of the mean field.** $x = 31$**,** $31.5$**,** $32$**,** $32.5$**,** $33$ **and** $33.5$**.** $\mathrm{Re} = 4000$ **and** $\alpha = 8°$**.**

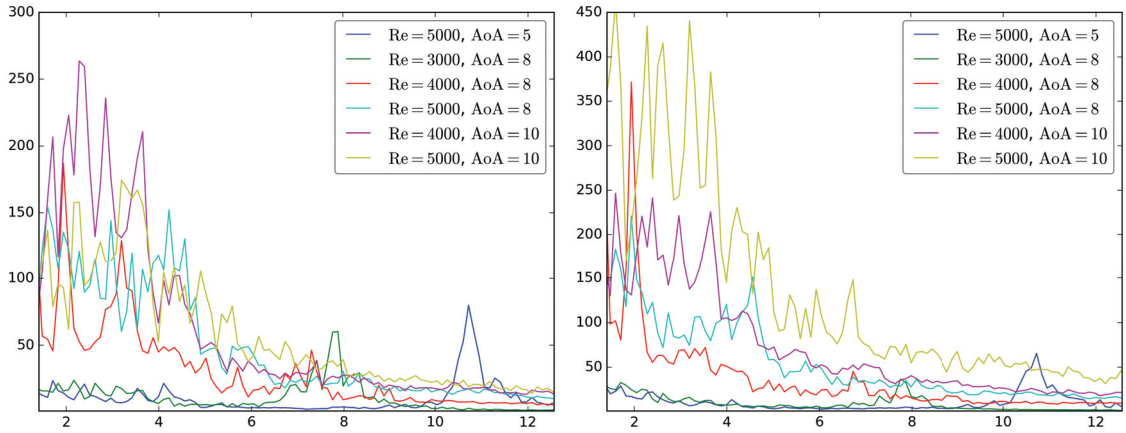


**Fig. 28 Amplitude of the vortex displacement as a function of the streamwise wavenumber of the (a) horizontal and (b) vertical vortex displacement around its mean position.**


[11] Brion, V., Sipp, D., and Jacquin, L., "Optimal amplification of the Crow instability," *Physics of Fluids*, Vol. 19, No. 11, 2007, p. 111703.

[12] Crouch, J. D., "Instability and transient growth for two trailing-vortex pairs," *Journal of Fluid Mechanics*, Vol. 350, 1997, p. 311–330.

[13] Fabre, D., and Jacquin, L., "Stability of a four-vortex aircraft wake model," *Physics of Fluids*, Vol. 12, No. 10, 2000, pp. 2438–2443.

[14] Fabre, D., Jacquin, L., and Loof, A., "Optimal perturbations in a four-vortex aircraft wake in counter-rotating configuration," *Journal of Fluid Mechanics*, Vol. 451, 2002, p. 319–328.

[15] Bristol, R., Ortega, J., Marcus, P., and Savas, Ö., "On cooperative instabilities of parallel vortex pairs," *Journal of Fluid Mechanics*, Vol. 517, 2004, pp. 331–358.

[16] Savas, Ö., "Experimental investigations on wake vortices and their alleviation," *Comptes Rendus Physique*, Vol. 6, No. 4, 2005, pp. 415–429.

[17] Widnall, S. E., Bliss, D. B., and Tsai, C.-Y., "The instability of short waves on a vortex ring," *Journal of Fluid Mechanics*, Vol. 66, No. 1, 1974, p. 35–47.

[18] Moore, D. W., and Saffman, P. G., "The instability of a straight vortex filament in a strain field," *Proc. R. Soc. Lond. A*, Vol. 346, No. 1646, 1975, pp. 413–425.

[19] LACAZE, L., RYAN, K., and LE DIZÈS, S., "Elliptic instability in a strained Batchelor vortex," *Journal of Fluid Mechanics*, Vol. 577, 2007, p. 341–361.

[20] Sipp, D., and Jacquin, L., "Widnall instabilities in vortex pairs," *Physics of Fluids*, Vol. 15, No. 7, 2003, pp. 1861–1874.

[21] Devenport, W. J., Zsoldos, J. S., and Vogel, C. M., "The structure and development of a counter-rotating wing-tip vortex pair," *Journal of Fluid Mechanics*, Vol. 332, 1997, p. 71–104.

[22] Roy, C., Leweke, T., Thompson, M. C., and Hourigan, K., "Experiments on the elliptic instability in vortex pairs with axial core flow," *Journal of Fluid Mechanics*, Vol. 677, 2011, pp. 383–416.

[23] Saffman, P. G., *Vortex dynamics*, Cambridge university press, 1992.

[24] Gupta, S., Zhao, J., Sharma, A., Agrawal, A., Hourigan, K., and Thompson, M. C., "Two- and three-dimensional wake transitions of a NACA0012 airfoil," *Journal of Fluid Mechanics*, Vol. 954, 2023, p. A26.

[25] Kurtulus, D. F., "On the wake pattern of symmetric airfoils for different incidence angles at Re = 1000," *International Journal of Micro Air Vehicles*, Vol. 8, No. 2, 2016, pp. 109–139.

[26] Deng, J., Sun, L., and Shao, X., "Wake dynamics of low-Reynolds-number flow around a two-dimensional airfoil," *Physics of Fluids*, Vol. 31, No. 2, 2019.

[27] Marquet, O., Leontini, J., Zhao, J., and Thompson, M., "Hysteresis of two-dimensional flows around a NACA0012 airfoil at Re=5000 and linear analyses of their mean flow." *International Journal of Heat and Fluid Flow*, Vol. 94, 2022, p. 108920.